Journal of Solid State Chemistry 182 (2009) 2430–2442

Contents lists available at ScienceDirect

Journal of Solid State Chemistry

journal homepage: www.elsevier.com/locate/jssc

Structure–composition sensitivity in "Metallic" Zintl phases: A study of $Eu(Ga_{1-x}Tt_x)_2$ (Tt = Si, Ge, $0 \le x \le 1$)

Tae-Soo You [a], Jing-Tai Zhao [b], Rainer Pöttgen [c], Walter Schnelle [d], Ulrich Burkhardt [d], Yuri Grin [d], Gordon J. Miller [a,*]

[a] Department of Chemistry, Iowa State University, Ames, IA 50011, USA
[b] Shanghai Institute of Ceramics, Chinese Academy of Sciences, 1295 Dingxi Road, Shanghai 200050, China
[c] Institut für Anorganische und Analytische Chemie, Universität Münster, Corrensstrasse 30, 48149 Münster, Germany
[d] Max-Planck-Institut für Chemische Physik fester Stoffe, Nöthnitzer Straße 40, 01187 Dresden, Germany

ARTICLE INFO

Article history:
Received 10 June 2009
Accepted 21 June 2009
Available online 27 June 2009

Keywords:
Polar intermetallics
Electronic structure
Crystallography

ABSTRACT

Two isoelectronic series, $Eu(Ga_{1-x}Tt_x)_2$ (Tt = Si, Ge, $0 \le x \le 1$), have been synthesized and characterized by powder and single-crystal X-ray diffraction, physical property measurements, and electronic structure calculations. In $Eu(Ga_{1-x}Si_x)_2$, crystal structures vary from the KHg_2-type to the AlB_2-type, and, finally, the $ThSi_2$-type structure as x increases. The hexagonal AlB_2-type structure is identified for compositions $0.18(2) \le x < 0.70(2)$ with Ga and Si atoms statistically distributed in the polyanionic 6^3 nets. As smaller Si atoms replace Ga atoms while the number of valence electrons increases, the lattice parameters, unit cell volumes, and Ga–Si distances in this phase region decrease significantly. Although aspects of X-ray diffraction results suggest puckering of the 6^3 nets for the Si-richest example of the AlB_2-type $Eu(Ga_{1-x}Si_x)_2$, the complete experimental evidence remains inconclusive. On the other hand, in $Eu(Ga_{1-x}Ge_x)_2$, six different structural types were observed as x varies. In addition to $EuGa_2$ (KHg_2-type; space group *Imma*) and $EuGe_2$ (own structure type, space group $P\bar{3}m1$), the ternary phases studied show four different structures: the AlB_2-type for Ga-rich compositions; the YPtAs-type structure for EuGaGe; and two new structures, which are intergrowths of the YPtAs-type EuGaGe and $EuGe_2$, for Ge-rich compositions. These two Ge-rich phases include: (1) $Eu(Ga_{0.45(2)}Ge_{0.55(2)})_2$ containing two YPtAs-type motifs of EuGaGe plus one $EuGe_2$ motif; and (2) $Eu(Ga_{0.40(2)}Ge_{0.60(2)})_2$ containing one YPtAs-type motif alternating with a split site at $x = \frac{2}{3}$, $y = \frac{1}{3}$ and $z = 0.4798(2)$ with ca. 50% site occupancy by Ga and Ge along the c-axis. Magnetic susceptibilities of three $Eu(Ga_{1-x}Ge_x)_2$ compounds display Curie–Weiss behavior above ca. 100 K, and show effective magnetic moments indicative of divalent Eu with a $4f^7$ electronic configuration, consistent with. X-ray absorption spectra (XAS). Density of states (DOS) and crystal orbital Hamilton population (COHP) analyses, based on first principles electronic structure calculations, rationalize the observed homogeneity ranges of the AlB_2-type phases in both systems and the structural variations as a function of Tt content.

1. Introduction

Polar intermetallic compounds represent an exceptional class of inorganic solids to study relationships among chemical compositions, crystal structures, physical properties, and chemical bonding [1]. These compounds involve electropositive metals (i.e., alkali-, alkaline-earth or rare-earth metals) combined with electronegative metals close to the Zintl border. The electronegative metals form structural fragments that often conform to simple electron counting rules, such as the Zintl-Klemm formalism [2–4], and give rise to electronic structures characterized by pseudogaps in the electronic density of states (DOS) curves and optimized orbital interactions at the corresponding Fermi levels [5–7]. On the other hand, the electropositive metals act like cations, which simply donate valence electrons to the electronegative components as in classical valence compounds or Zintl phases. In polar intermetallic compounds, however, the active metals do not transfer all valence electrons to the electronegative component, but are involved in "lattice covalency" through their valence orbitals [8]. This effect was recently demonstrated between Eu and its environment in $EuRh_2Ga_8$ by means of a bonding analysis within the electron localization approach [9]. In addition, the typical presence of a pseudogap at the Fermi level can lead to potentially interesting physical properties, especially if rare-earth metals serve as the active metal, because of partially filled 4*f* bands [10].

* Corresponding author.
E-mail address: gmiller@iastate.edu (G.J. Miller).

0022-4596/$ - see front matter © 2009 Elsevier Inc. All rights reserved.
doi:10.1016/j.jssc.2009.06.032

During our systematic investigations of $Eu(M_{1-x}M'_x)_2$ phases (M, M' = group 12–14 elements) to study correlations among atomic, electronic, and possible magnetic structures by varying atomic sizes and valence electron counts, we observed different structural trends for two isoelectronic $Eu(Ga_{1-x}Tt_x)_2$ (Tt = Si, Ge) series. As x increases in $Eu(Ga_{1-x}Si_x)_2$, structures vary from the KHg_2-type to the AlB_2-type, and, finally, the $ThSi_2$-type structure type. On the other hand, six different structural types exist in the germanide system, $Eu(Ga_{1-x}Ge_x)_2$. In addition to the two binary cases, $EuGa_2$ (KHg_2-type) and $EuGe_2$, ternary examples show four different structures derived from the AlB_2-motif. These ternary AlB_2-type compounds are related to the superconducting *AE*AlSi (*AE* = Ca and Sr) phases [11–15], which have attracted recent attention for their similarity to superconducting MgB_2 [16] with respect to structures and valence electron counts. Moreover, related ternary phases *AE*Ga*Tt* (*AE* = Ca, Sr, Ba; *Tt* = Si, Ge, Sn) are precursors to form interesting polyanionic hydrides [17]. In our own previous investigations, we have characterized and analyzed the influence of the atomic size factor [18] and valence electron count [19,20] on the structural and chemical bonding features of the 6^3 networks, respectively, for EuGa*Tt* (*Tt* = Si, Ge, Sn) [18] and $Eu(Zn_{1-x}Ge_x)_2$ ($0 \le x \le 1$) [19,20]. In this work, we examine the simultaneous influence of size and electronic factors on the $Eu(Ga_{1-x}Tt_x)_2$ (Tt = Si, Ge, $0 \le x \le 1$) series.

2. Experimental

2.1. Synthesis and chemical analysis

Members of the $Eu(Ga_{1-x}Tt_x)_2$ (Tt = Si, Ge, $0 \le x \le 1$) series were synthesized from the pure elements, Eu (Ames Laboratory, rod, 99.99%, or Johnson-Matthey, >99.9%), Ga (Ames Laboratory, ingot, 99.99% or Chempur, >99.99%), Si (Aldrich, piece, 99.999%), and Ge (Alfa, piece, 99.999% or Wacker, >99.999%) in various molar ratios targeting sample masses of 1.0 ± 0.2 g.

2.2. $Eu(Ga_{1-x}Si_x)_2$

Eight different $Eu(Ga_{1-x}Si_x)_2$ ($0 \le x \le 1$) samples were arc-melted under a high purity argon atmosphere on a water-cooled copper hearth. Each pellet was remelted six times after turning to ensure homogeneity. Weight losses of ca. 0.4–0.7 wt% occurred during arc-melting, but these losses did not affect the final targeted compositions, being equally distributed among the three components as determined by subsequent chemical analysis and refinements of single-crystal X-ray diffraction experiments [18]. Moreover, samples prepared using either a radio-frequency (RF) induction furnace (1500 °C for 15 min followed by 2 h at 650 °C) or a conventional tube furnace (tantalum ampoules; 850 °C for 4 days, 450 °C for 1 week, naturally cooled to room temperature) yielded identical products, but crystals extracted from these samples were less suitable for subsequent diffraction experiments and the samples often showed other phases. $EuGa_2$ was readily synthesized by arc-melting without any subsequent low-temperature annealing procedure, unlike original reports [21,22], but in agreement with a recent publication [23]. On the basis of powder X-ray diffraction patterns, all samples obtained simply by arc-melting showed features suitable to pursue subsequent single-crystal X-ray diffraction experiments without any further annealing.

2.3. $Eu(Ga_{1-x}Ge_x)_2$

Seven of eight $Eu(Ga_{1-x}Ge_x)_2$ ($0 \le x \le 1$) samples were prepared using RF induction melting at 1300 °C with a holding time of 15 min. Reactant mixtures were loaded into tantalum ampoules, which were sealed by arc-melting in an argon-filled glove box with the concentration of O_2 lower than 1 ppm. Each tantalum ampoule was then sealed in an evacuated silica jacket to prevent oxidation. After annealing each product at 350 °C for 1 week, there were no observable changes in the X-ray diffraction patterns, except for the one sample $Eu(Ga_{0.50(2)}Ge_{0.50(2)})_2$, which showed significant narrowing of the diffraction peaks by factors of 2–2.5 compared with the as cast sample. $EuGa_{1.1}Ge_{0.9}$ was prepared in a sealed tantalum tube. The sample was first heated in a muffle furnace at 1050 °C for 1 h, then cooled to 700 °C within 1 day and kept at that temperature for another 7 days followed by quenching.

All 16 samples of the $Eu(Ga_{1-x}Tt_x)_2$ series (Tt = Si, Ge, $0 \le x \le 1$) appeared to be stable on exposure to both air and moisture over several weeks. Empirical formulas obtained from single-crystal X-ray diffraction experiments were verified by energy-dispersive X-ray spectroscopy (EDXS). EDXS analysis was conducted on a Hitachi S-2460N variable-pressure scanning electron microscope (SEM) equipped with an Oxford Instruments Link Isis Model 200 X-ray analyzer, and using samples that were investigated by single-crystal X-ray diffraction. The pure elements were used as standards for intensity references.

2.4. Crystal structure determinations

The $Eu(Ga_{1-x}Tt_x)_2$ (Tt = Si, Ge, $0 \le x \le 1$) series were characterized at room temperature by both powder and single-crystal X-ray diffraction. Phase analysis and lattice parameters were determined on a Huber 670 image-plate powder diffraction camera (Cu $K\alpha_1$ radiation, $\lambda = 1.54059$ Å) with a step size of 0.005°, exposure times of 1–2 h, and using Si powder (NIST; $a = 5.430940 \pm 0.000035$ Å) as a standard. Data acquisition was controlled via the *in situ* program. The lattice parameters were obtained from Rietveld refinement using program *Rietica* [24].

For single-crystal X-ray diffraction experiments, several silvery block- or plate-shaped crystals were selected from the cast of each product. The quality of each crystal was checked by a rapid scan on a Bruker SMART Apex CCD diffractometer with Mo $K\alpha_1$ radiation ($\lambda = 0.71073$ Å), and then the best crystals were used for further data collection. Diffraction data were harvested from three sets of 606 frames on a full sphere with 0.3° scans in ω and with an exposure time of 10–20 s per frame. For experiments conducted on a STOE IPDS diffractometer, data were harvested from two sets of 180 frames with an exposure time of 1–3 min per frame. Data collection on the STOE STADI 4 machine was completed in $\theta/2\theta$ mode.

Intensities were extracted and then corrected for Lorentz and polarization effects using the *SAINT* program [25]. The program *SADABS* [26] was used for empirical absorption correction. Numerical absorption corrections were applied using the *X-RED*/*X-SHAPE* program [26]. All structures were solved by direct methods and refined on F^2 by full-matrix least-squares methods using the *SHELXTL* [27] or *WinCSD* [28] software packages. The entire sets of reflections for the ternary $Eu(Ga_{1-x}Tt_x)_2$ (Tt = Si, Ge, $0 \le x \le 1$) series could be matched with hexagonal or trigonal crystal systems. During refinements of $Eu(Ga_{1-x}Ge_x)_2$ ($0.25 \le x \le 0.60$), the Ga and Ge atoms could not be distinguished given the X-ray scattering factors for Ga and Ge atoms which differ by at most 3.1%. Moreover, interatomic distances were also not a useful guide to distinguish Ga and Ge atoms, due to their similar covalent radii: r(Ga) = 1.25 Å and r(Ge) = 1.22 Å [29]. However, electronic structure calculations performed on several different models of EuGaGe provided a clear energetic minimum for one atomic arrangement in EuGaGe [18], which agreed with

structural characterization of EuGaSn. Therefore, we utilized similar calculations to address these structures and their compositions.

2.5. X-ray absorption spectroscopy (XAS)

XAS measurements on the Eu L_{III} edge of four $Eu(Ga_{1-x}Ge_x)_2$ ($x = 0.45(5)$, 0.50(2), 0.55(2), 0.60(2)) samples were examined at the EXAFS beam-line A1 of HASYLAB at DESY (Hamburg, Germany). Each sample was ground together with dry B_4C powder before the measurement. Wavelength selection was realized by means of a double-crystal Si(111) monochromator. Resolution was about 2 eV (fwhm) at the Eu L_{III} edge of 6977 eV. Eu_2O_3 was used as a reference for the $4f^6$ threshold during the measurement.

2.6. Magnetic susceptibility measurements

Temperature- and magnetic field-dependent magnetic susceptibilities of $Eu(Ga_{1-x}Ge_x)_2$ ($x = 0.50(2)$, 0.55(2), 0.60(2)) samples were measured using a Quantum Design, MPMS XL-7 SQUID magnetometer over the temperature range 1.8–400 K and in magnetic fields $\mu_0 H = 0.01$–7 T. Isothermal magnetization curves up to $\mu_0 H = 7$ T were recorded at 1.8 K. Bulk samples (ca. 100 mg) from the same preparation as the one used for powder diffraction experiments were used.

Table 1
Crystallographic data as determined by XPD for the $Eu(Ga_{1-x}Si_x)_2$ and $Eu(Ga_{1-x}Ge_x)_2$ ($0 \le x \le 1$) series.

x (loaded)	x (EDXS)	Structure type	a (Å)	b (Å)	c (Å)	$(c/a)^*$	V^* (Å^3)
$Eu(Ga_{1-x}Si_x)_2$ phases							
0	0.00	KHg_2	4.6449(9)	7.628(2)	7.638(2)	0.8211	67.65(2)
0.18	0.16(2)	KHg_2	4.6524(5)	7.6461(9)	7.6464(8)	0.8127	68.00(1)
		AlB_2	4.2640(2)		4.6000(2)	1.0788	72.45(5)
0.26	0.29(2)	AlB_2	4.2324(3)		4.5885(4)	1.0841	71.17(1)
0.30	0.33(2)	AlB_2	4.2204(2)		4.5863(2)	1.0867	70.75(1)
0.50	0.50(2)	AlB_2	4.1699(5)		4.5634(6)	1.0946	68.72(2)
0.67	0.69(2)	AlB_2	4.1132(3)		4.5412(4)	1.1041	66.53(1)
0.84	0.82(2)	AlB_2	4.0821(1)		4.5538(3)	1.1156	65.72(3)
		$ThSi_2$	4.2989(4)		13.864(2)		64.06(1)
1.00	1.00(2)	$ThSi_2$	4.3065(4)		13.683(1)	–	63.44(1)
$Eu(Ga_{1-x}Ge_x)_2$ phases							
0	0.00	KHg_2	4.6449(9)	7.628(2)	7.638(2)	0.8211	67.65(2)
0.25	0.25(2)	AlB_2	4.2905(5)		4.6077(2)	1.0739	73.46(1)
0.35	0.35(2)	AlB_2	4.2617(2)		4.5812(2)	1.0749	72.06(1)
0.45	0.45(2)	AlB_2	4.241(1)		4.555(1)	1.079	70.95(5)
0.50	0.50(2)	YPtAs	4.2655(6)		18.034(2)	1.0569	71.04(2)
0.55	0.55(2)	$EuGa_{0.9}Ge_{1.1}$	4.2537(6)		40.889(8)	1.0681	71.18(3)
0.60	0.60(2)	$EuGa_{0.8}Ge_{1.2}$	4.2320(1)		22.974(1)	1.0857	71.27(2)
1.00	1.00(2)	$EuGe_2$	4.1044(4)		4.9996(1)	1.2181	72.94(3)

V^* = volume per formula unit $Eu(Ga_{1-x}Tt_x)_2$. $(c/a)^*$ is c/a for a AlB_2-type unit cell, $b/2a$ for a KHg_2-type unit cell, $c/4a$, for a YPtAs-type unit cell, $c/9a$ for a $EuGa_{0.9}Ge_{1.1}$-type unit cell, and $c/5a$ for a $EuGa_{0.8}Ge_{1.2}$-type unit cell.

2.7. Computational details

Tight-binding, linear muffin-tin orbital (TB-LMTO) calculations of various structural models of $Eu(Ga_{1-x}Si_x)_2$ and $Eu(Ga_{1-x}Ge_x)_2$ were carried out in the atomic sphere approximation (ASA) using the Stuttgart program [30]. Exchange and correlation were treated by the local spin density approximation (LSDA) [31]. All relativistic effects except spin–orbit coupling were taken into account by using a scalar relativistic approximation [32]. In the ASA method, space is filled with overlapping Wigner–Seitz (WS) atomic spheres. The symmetry of the potential is considered spherical inside each WS sphere, and a combined correction is used to take into account the overlapping part [33]. The radii of WS spheres were obtained by requiring that the overlapping potential be the best possible approximation to the full potential, and were determined by an automatic procedure [33]. No empty spheres (ES) were used [30]. The WS radii for the various elements covered the following ranges: Eu, 2.09–2.26 Å; Ga, 1.30–1.52 Å; Si, 1.33 Å; and Ge, 1.46–1.51 Å. More computational details are included in Supporting Information (Table S2). The basis sets included 6*s*, 6*p*, and 5*d* orbitals for Eu; 4*s*, 4*p*, and 4*d* orbitals for Ga; 3*s*, 3*p*, and 3*d* orbitals for Si; 4*s*, 4*p*, and 4*d* orbitals for Ge. The Eu 6*p*, Ga 4*d*, Si 3*d*, and Ge 4*d* orbitals were treated by the Löwdin downfolding technique [30–32], and the Eu 4*f* wave functions were treated as core functions occupied by 7 electrons. This assigns all Eu sites as formally Eu(II), which is consistent with the results of physical property measurements. Crystal orbital Hamilton population (COHP) curves [6] and integrated COHP values (ICOHPs) were calculated to determine the relative influences of various interatomic orbital interactions. *k*-Space integrations were performed by the tetrahedron method [34]. The self-consistent charge densities were obtained using 116–560 irreducible *k*-points in the Brillouin zones for the corresponding unit cells.

Total energy calculations using the *Vienna ab initio Simulation Package* (VASP) [35–37] were also conducted for various $EuSi_2$ models to gain insights about the Si-rich end of AlB_2-type $Eu(Ga_{1-x}Si_x)_2$ cases. In this approach, the Kohn–Sham equations were solved self-consistently using an iterative matrix diagonalization method and an efficient Pulay mixing scheme of the charge density [37]. For these calculations on $EuSi_2$, the free parameters of the Si positions and the lattice parameter ratios c/a for a set of constant volumes were varied simultaneously until forces converged to values less than 0.005 eV/Å. Ultrasoft Vanderbilt-type pseudopotentials [38,39] were employed, and the valence electron configurations of Eu and Si involved, respectively, $5d^1 6s^2$ and $3s^2 3p^2$. Convergency was checked with

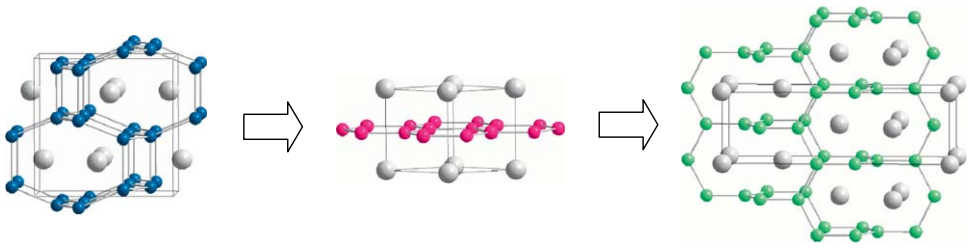

Fig. 1. Concentration-induced changes of crystal structure in the $Eu(Ga_{1-x}Si_x)_2$ ($0 \le x \le 1$) series. The electron numbers show valence electron count per formula unit $Eu(Ga_{1-x}Si_x)_2$ (Eu is counted as contributing two valence electrons).

respect to the plane-wave cutoff of 300 eV and the number of *k*-points used in the summation over the Brillouin zone, *k*-points which were obtained by the Gamma-Pack method and sampled on a dense $32 \times 32 \times 32$ grid.

3. Results and discussion

3.1. Crystal structures and compositions

Table 1 summarizes the phase analyses of $Eu(Ga_{1-x}Tt_x)_2$ (Tt = Si, Ge) in this study based on EDXS and X-ray powder diffraction (XPD). Nearly all $Eu(Ga_{1-x}Si_x)_2$ and $Eu(Ga_{1-x}Ge_x)_2$ phases adopt structures based on eclipsed stackings of planar or puckered 6^3 $[Ga_{1-x}Tt_x]$ nets; the only exceptions are silicides at and near the composition $EuSi_2$, which show three-dimensional 3-connected tetragonal nets of locally trigonally planar Si atoms [40]. The other binary phases, $EuGa_2$ and $EuGe_2$, contain eclipsed stackings of puckered 6^3 nets: in $EuGa_2$ [41], Ga atoms form a three-dimensional 4-connected net with each Ga atom surrounded by a distorted tetrahedral environment [23]; whereas, in $EuGe_2$ [42,43], Ge atoms create a two-dimensional 3-connected net with each Ge atom in trigonal pyramidal surroundings. As the results in Table 1 indicate, $Eu(Ga_{1-x}Tt_x)_2$ phases for low Si or Ge content, x, adopt the hexagonal AlB_2-type structure with apparently statistical distributions of Ga and Tt atoms throughout the planar 6^3 nets. Furthermore, the unit cell volumes per formula unit for these AlB_2-type phases are *larger* than that for $EuGa_2$, and show decreasing volumes with increasing Tt content x. When x reaches and slightly exceeds 0.50 in $Eu(Ga_{1-x}Tt_x)_2$, puckering of the 6^3 $[Ga_{1-x}Tt_x]$ nets becomes clearly evident in the germanides, but not for the silicides. In the silicides, the volume per formula unit monotonically decreases through $EuSi_2$; in the germanides, the volume passes through a minimum near $x = 0.55$ for $Eu(Ga_{1-x}Ge_x)_2$. These peculiarities in the $Eu(Ga_{1-x}Tt_x)_2$ series were further examined by both single-crystal diffraction and theoretical calculations.

3.2. $Eu(Ga_{1-x}Si_x)_2$

Three different structure types (Fig. 1) were identified along the entire $Eu(Ga_{1-x}Si_x)_2$ series, as seen in XPD patterns (Fig. 2). Among ternary cases, single-phase products appear for the four loaded compositions ranging from $x = 0.26$ to 0.67 and could be indexed by the hexagonal AlB_2-type structure, space group $P6/mmm$. In all cases, no commensurately or incommensurately modulated structures were observed in the XPD patterns nor were they apparent from single-crystal diffraction. Thus, Ga and Si atoms refined to occupy the 2*d* sites statistically, with results that are consistent with both loaded compositions and EDXS analyses. Table 2 summarizes crystallographic results from single-crystal diffraction experiments recorded on samples extracted from the single-phase AlB_2-type products.

Two-phase regions surround this single-phase region based on XPD patterns of the loaded compositions $x = 0.18$ and 0.84. Both of these XPD patterns (Fig. 2b and e) contain reflections consistent with an AlB_2-type phase, although analysis of the Si-rich sample ($x = 0.84$) suggests some puckering of the 6^3 net (see subsequent discussion). The remaining reflections in each of these samples could be matched with the structure type of the corresponding binary phase, i.e., either orthorhombic KHg_2-type $EuGa_2$ [41] for $x = 0.18$ or tetragonal $ThSi_2$-type $EuSi_2$ [40] for $x = 0.84$, but with lattice parameters sufficiently different from each binary phase, respectively, to suggest a small degree of mutual replacements of Ga and Si atoms in each binary phase. KHg_2-type $Eu(Ga_{1-x}Si_x)_2$ in

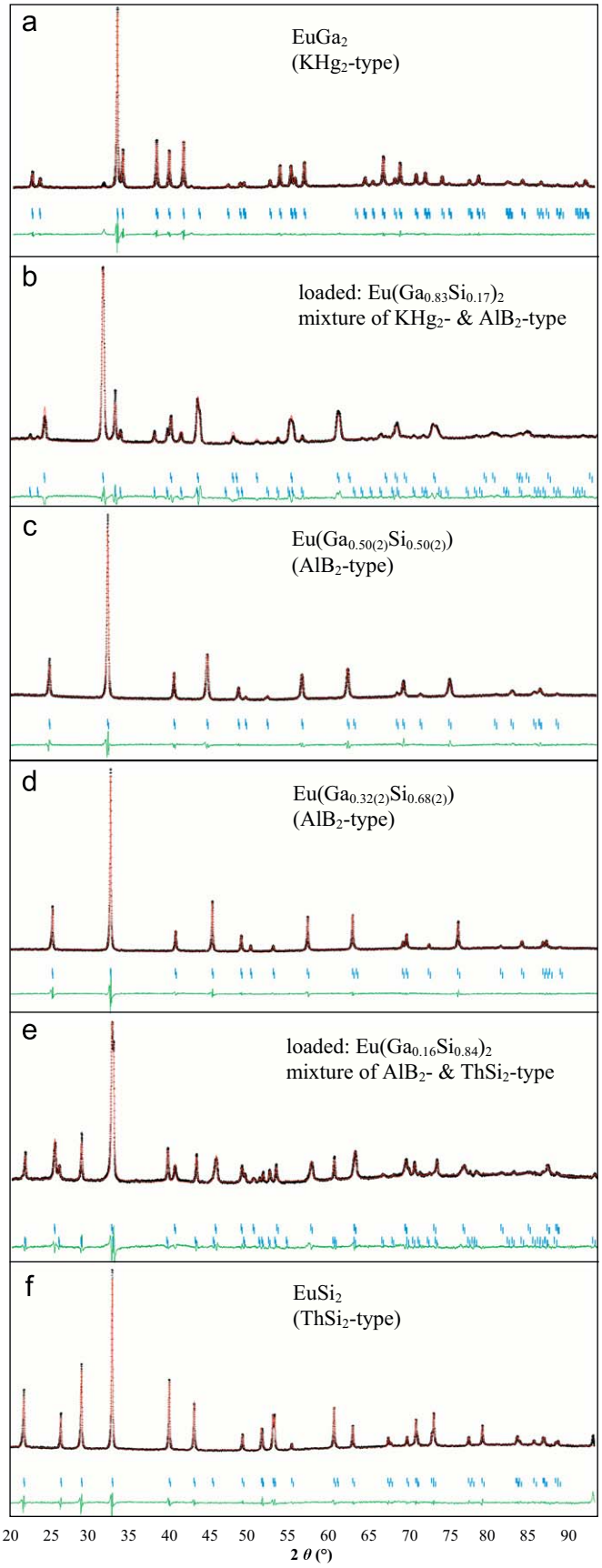

Fig. 2. XPD patterns of selected samples of the $Eu(Ga_{1-x}Si_x)_2$ ($0 \le x \le 1$) series. For the two-phase samples (b) and (e), reflection positions for the AlB_2-type phase are noted below the diffraction pattern.

Table 2
Crystallographic data for $Eu(Ga_{1-x}Si_x)_2$ (structure type AlB_2, space group $P6/mmm$).

Loaded composition		$Eu(Ga_{0.74}Si_{0.26})_2$	$Eu(Ga_{0.70}Si_{0.30})_2$	$Eu(Ga_{0.50}Si_{0.50})_2$	$Eu(Ga_{0.33}Si_{0.67})_2$
EDXS composition		$Eu(Ga_{0.71}Si_{0.29(1)})_2$	$Eu(Ga_{0.67}Si_{0.33(1)})_2$	$Eu(Ga_{0.50}Si_{0.50(1)})_2$	$Eu(Ga_{0.31}Si_{0.69(1)})_2$
Refined composition		$Eu(Ga_{0.72}Si_{0.28(2)})_2$	$Eu(Ga_{0.67}Si_{0.33(2)})_2$	$Eu(Ga_{0.50}Si_{0.50(2)})_2$	$Eu(Ga_{0.32}Si_{0.68(2)})_2$
Formula weight ($g\,mol^{-1}$)		267.18	263.91	249.77	233.95
c/a		1.0841	1.0867	1.0946	1.1041
Volume ($Å^3$)		71.17(1)	70.75(1)	68.72(2)	66.53(1)
Density calc. ($g\,cm^{-3}$)		5.80	5.85	6.04	5.90
Diffractometer		STOE IPDS	SMART Apex	STOE IPDS	STOE IPDS
2θ range (deg)		8.90–68.4	8.9–70.04	8.94–69.72	8.98–69.44
Index ranges		$-6\le h\le 6$, $-6\le k\le 6$, $-6\le l\le 7$	$-6\le h\le 6$, $-6\le k\le 6$, $-7\le l\le 7$	$-6\le h\le 6$, $-6\le k\le 6$, $-7\le l\le 7$	$-6\le h\le 5$, $-6\le k\le 6$, $-7\le l\le 6$
Reflections collected		1263	1020	1030	1312
Independent reflections		86 [$R_{init}=0.049$]	89 [$R_{init}=0.021$]	87 [$R_{init}=0.017$]	84 [$R_{init}=0.066$]
Data/refined parameters		86/7	89/7	87/7	84/7
GOF on F^2		1.192	1.146	1.190	1.173
R indices (all data)		$R_1=0.021$, $wR_2=0.059$	$R_1=0.010$, $wR_2=0.024$	$R_1=0.009$, $wR_2=0.022$	$R_1=0.013$, $wR_2=0.032$
Largest diff. peak and hole ($e^-/Å^3$)		1.57/−1.81	0.48/−0.63	0.67/−0.41	0.44/−0.78
U_{eq} ($Å^2$)	Eu (1*a*)	0.017(1)	0.011(1)	0.010(1)	0.015(1)
	Ga/Si (2*d*)	0.021(1)	0.013(1)	0.016(1)	0.027(1)
U_{33}/U_{11}	Eu (1*a*)	0.7	0.8	0.9	0.8
	Ga/Si (2*d*)	1.5	2.7	3.8	3.7
d (Ga/Si–Ga/Si) (Å)		2.4436(2)	2.4366(1)	2.4075(3)	2.3748(2)
d (Eu–Ga/Si) (Å)		3.3518(2)	3.3460(1)	3.3170(4)	3.2856(2)

the $x=0.18$ sample shows a volume expansion of ca. 0.5% compared to that of $EuGa_2$; $ThSi_2$-type $Eu(Ga_{1-x}Si_x)_2$ in the $x=0.84$ sample shows a volume expansion of ca. 1.0% compared to that of $EuSi_2$.

For the single-phase AlB_2-type $Eu(Ga_{1-x}Si_x)_2$ products, the lattice parameters and unit cell volumes decrease linearly with x as smaller Si atoms replace Ga atoms (covalent radii: $r(Si)=1.17$ Å, $r(Ga)=1.25$ Å) [29]. Fig. 3 illustrates the trend in unit cell volumes vs. refined Si content x with the dashed line indicating the linear fit for the four single-phase samples (black dots). The Ga/Si–Ga/Si (2*d*–2*d*) distances, which are proportional to the *a* parameters, decrease with increasing Si content in excellent agreement with statistical occupation of the 2*d* sites: e.g., for $Eu(Ga_{0.72}Si_{0.28(2)})_2$, the experimental distance of 2.440(2) Å compares favorably with the value 2.455 Å as predicted from the covalent radii; for $Eu(Ga_{0.32}Si_{0.68(2)})_2$, the distance is 2.375(1) Å, as compared to the expected value of 2.390 Å. Furthermore, the Ga/Si–Ga/Si (2*d*–2*d*) distance of 2.375(1) Å in $Eu(Ga_{0.32}Si_{0.68(2)})_2$ is slightly smaller than the average Si–Si distance in $EuSi_2$ (2.383 Å; based on 2.306 Å (1×) and 2.421 Å (2×) [40]). Moreover, the *a* parameters drop faster than the *c* parameters with increasing x, so that the c/a ratios increase with increasing Si content. These two structural features suggest that the 6^3 $[Ga_{1-x}Si_x]$ nets in AlB_2-type $Eu(Ga_{1-x}Si_x)_2$ phases could become puckered at higher Si levels.

Puckering of the 6^3 $[Ga_{1-x}Si_x]$ nets in $Eu(Ga_{1-x}Si_x)_2$ was not apparent in the results from single-crystal diffraction experiments on crystals extracted from the single-phase AlB_2-type products (see Table 2), although the U_{33}/U_{11} ratio of the 2*d* (Ga/Si) site steadily increases from 1.5 in $Eu(Ga_{0.72}Si_{0.28(2)})_2$ to 3.7 in $Eu(Ga_{0.32}Si_{0.68(2)})_2$. Structural refinements of these phases in the space group $P\bar{3}m1$, which allows the *z*-coordinate of the 2*d* site to be varied, keep this coordinate at 1/2. Nevertheless, the XPD patterns of all AlB_2-type phases, including those observed in the two-phase patterns (Fig. 2b and e), reveal the reflection intensity ratios $I(0\,0\,1)/I(0\,0\,2)$ and $I(1\,1\,0)/I(0\,0\,2)$ increase as the Si content increases. Simulated XPD patterns based on planar (AlB_2-type, space group $P6/mmm$) and puckered ($EuGe_2$-type, space group $P\bar{3}m1$) $^2_\infty[Ga_{1-x}Si_x]$ nets suggest that the pattern observed in the two-phase diagram (Fig. 2e), which was obtained by loading $x=0.84$ for $Eu(Ga_{1-x}Si_x)_2$ could be *better attributed to a puckered* 6^3 *net*. On the other hand, the XPD diagrams for all other AlB_2-type samples are better modeled by planar 6^3 nets. Linear extrapolation of the curve in Fig. 3 to lower x values gives $x=0.18(3)$ for the AlB_2-type phase in the two-phase Ga-rich sample. A comparable extrapolation at the Si-rich end estimates $x=0.75(3)$ for the corresponding phase in the two-phase Si-rich sample. However, since the XPD patterns suggest different structures for $Eu(Ga_{0.32}Si_{0.68(2)})_2$ and $Eu(Ga_{0.25}Si_{0.75(3)})_2$, we *estimate* the observed range for AlB_2-type $Eu(Ga_{1-x}Si_x)_2$ phases to be $0.18(2)\le x<0.70(2)$. Subsequent theoretical calculations corroborate this conclusion. Moreover, related work on EuT_xSi_{2-x} (T = Fe, Co, Ni, Cu, Ag, Au) achieved similar results, but with limited ranges for single-phase products [44].

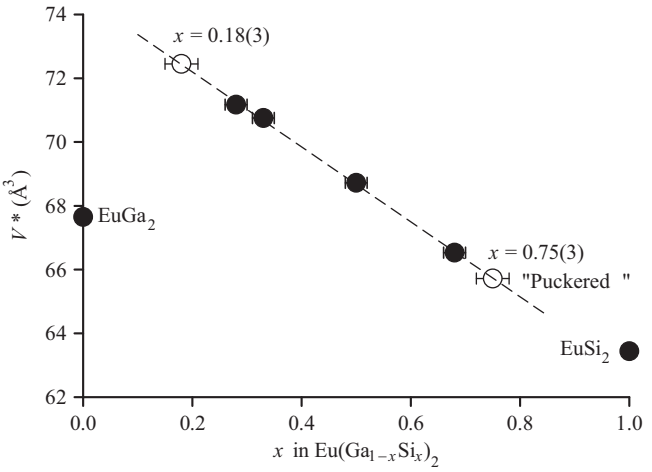

Fig. 3. Variation in unit cell volume with composition for the $Eu(Ga_{1-x}Si_x)_2$ samples identified as single-phase products (see Table 1). The dashed line is the linear fit to the four phases shown as black dots. Open circles indicate the volumes of the AlB_2-type phases observed in the two-phase samples; corresponding x values are determined by extrapolating the linear fit (see text for further discussion).

3.3. $Eu(Ga_{1-x}Ge_x)_2$

The germanide series differs from the analogous silicides by exhibiting puckered hexagonal variants of the AlB_2 structure type, which are also commensurately modulated along the *c*-axis. This difference may be due, in part, to the ground state structure of $EuGe_2$ (space group $P\bar{3}m1$), which is the simplest puckered derivative of the AlB_2 structure [42], as compared to the tetragonal structure of $EuSi_2$. Loaded compositions for $Eu(Ga_{1-x}Ge_x)_2$ ranged from $x = 0.25$ to 0.60; no multi-phase products were detected by XPD (see Fig. 4).

Three Ga-rich samples, $Eu(Ga_{0.75}Ge_{0.25(2)})_2$, $Eu(Ga_{0.65}Ge_{0.35(2)})_2$, and $Eu(Ga_{0.55}Ge_{0.45(2)})_2$, crystallize in the AlB_2-type structure (Fig. 5) with decreasing lattice parameters as the Ge content increases; the XPD pattern of $Eu(Ga_{0.75(2)}Ge_{0.25(2)})_2$ is shown in Fig. 4a. As in the analogous $Eu(Ga_{1-x}Si_x)_2$ phases, we assume that the Ga and Ge atoms are statistically distributed at the 2*d* site, as there is no evidence to suggest any in-plane or out-of-plane ordering of Ga and Ge atoms throughout the structure. Furthermore, we did observe deviation of atoms in the 2*d* sites away from the *ab*-mirror plane (i.e., $z \neq \frac{1}{2}$) as the Ge content increases. Refinement of the crystal structure of $Eu(Ga_{0.55(5)}Ge_{0.45(5)})_2$ with Ga in the 2*d* position yielded a relatively good residual ($R_F = 0.0491$), but revealed extreme anisotropy of the displacement parameters ($U_{33}/U_{11} = 12$). This clearly suggested a disorder around the 2*d* site, which was confirmed by calculating the difference electron density in the vicinity of this position (Fig. 6a). Location of a Ga or Ge atom at $z = \frac{1}{2}$ takes into account only part of the experimental density; some unaccounted density is observed along [0 0 1] below and above this region (Fig. 6b). If the Ga or Ge atom is located at $z = 0.56$ (4*h* site) with one-half occupation, the experimental data are better described than the previous case (cf. absolute values in Fig. 6b and c). Nevertheless, a small residual density remains at $z = \frac{1}{2}$ (Fig. 6c). The difference density map without noticeable maxima was observed only by locating Ga or Ge atoms in both positions with different occupations (Fig. 6d). This also reduced the residuals remarkably ($R_F = 0.0239$) as compared to the primary anisotropic refinement above. Table 3 includes the crystallographic results for these three specimens.

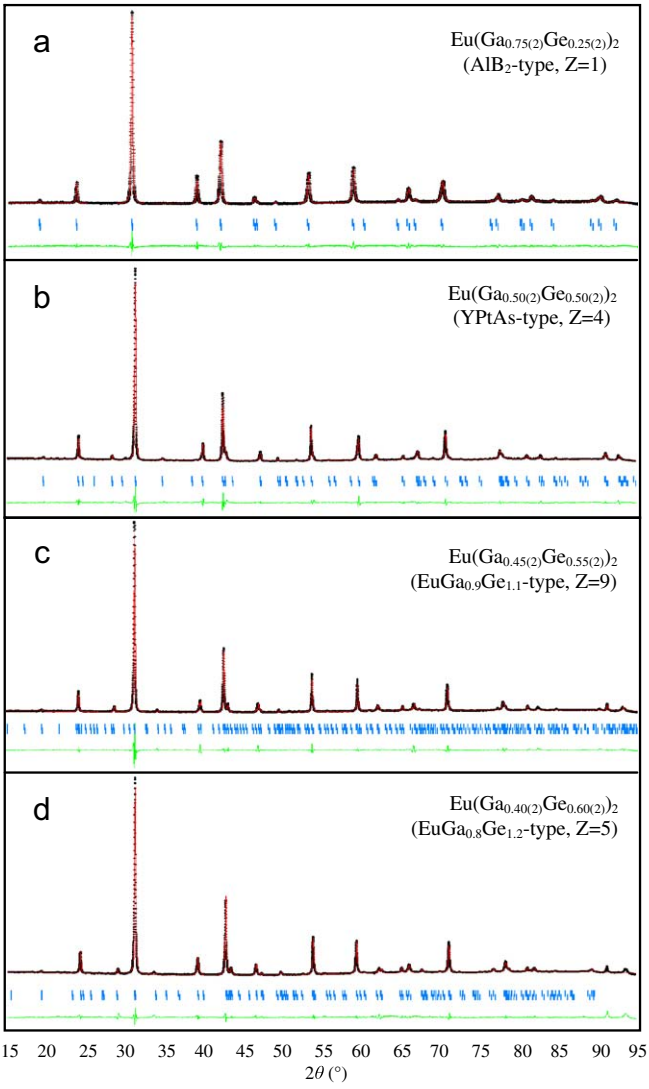

Fig. 4. XPD patterns of $Eu(Ga_{1-x}Ge_x)_2$ ($x = 0.25(2)$, 0.50(2), 0.55(2), 0.60(2)). *Z* indicates the number of formula units $Eu(Ga_{1-x}Ge_x)_2$ in one unit cell (see also Fig. 5).

At the equiatomic ratio, EuGaGe adopts the YPtAs-type structure, which is a puckered, ordered, ternary derivative of the AlB_2-type yielding a quadrupled *c* parameter because of the stacking sequence of the 6^3 nets (see also Fig. 5) [18]. The diffraction peaks in Fig. 4b that differentiate the YPtAs-type from the related AlB_2-type are clearly detected at $2\theta = 28.62°$, 34.33°, and 62.03°. As we discussed previously [18], the Ga and Ge atoms alternate in each 6^3 net, and adjacent nets are puckered to locate Ga atoms closer to each other. Nevertheless, in EuGaGe, this Ga···Ga distance remains quite long, ca. 3.726 Å. The distribution of Ga and Ge atoms could not be conclusively determined from experiment, but was assigned from comparison with the EuGaSn analogue as well as computational results.

For *x* exceeding 0.50 in $Eu(Ga_{1-x}Ge_x)_2$, two new phases, $Eu(Ga_{0.45}Ge_{0.55(2)})_2$ and $Eu(Ga_{0.40}Ge_{0.60(2)})_2$, have been discovered and adopt distinct, yet related complex structures, which can also be described as puckered derivatives of the AlB_2-type structure. $Eu(Ga_{0.45}Ge_{0.55(2)})_2$ contains nine puckered 6^3 nets stacked along the *c*-axis (see Fig. 5). Among these nine layers, eight show stacking environments similar to those in EuGaGe (YPtAs-type) and one resembles the stacking of 6^3 nets in $EuGe_2$. Thus, during refinement, we assigned alternating Ga and Ge atoms to the EuGaGe-type nets and Ge atoms only to the remaining puckered net. This assignment agrees with the results of EDXS measurements and the loaded composition. Therefore, the structure of $Eu(Ga_{0.45}Ge_{0.55(2)})_2$ is a 2:1 intergrowth of two YPtAs-type EuGaGe unit cells (each unit cell of this type contains 4 EuGaGe formulas) with one $EuGe_2$ unit cell, which can be formulated as $[(EuGaGe)_4]_2[EuGe_2]$ = "$Eu_9Ga_8Ge_{10}$" = $Eu(Ga_{0.44}Ge_{0.56})_2$. The corresponding Ga···Ga distances between adjacent 6^3 [GaGe] nets in the EuGaGe portions are also much longer than expected for significant covalently bonded interactions, i.e., 3.676(1) and 3.995(1) Å.

On the other hand, the unit cell of $Eu(Ga_{0.40}Ge_{0.60(2)})_2$, contains five puckered 6^3 nets stacked along the *c*-axis in the unit cell. During refinement in the space group $P\bar{6}m2$, an anomalously large U_{33} parameter occurred for one 1*f* site at (2/3, 1/3, 1/2), so we refined this site as split into two symmetrically identical 2*i* sites with ca. 50% Ga or Ge site occupancies at (2/3, 1/3, 0.4798(2)). This solution creates two differently puckered 6^3 nets, which are disordered in a 50:50 ratio along the *c*-axis; the remaining four layers are well behaved. Alternative refinement strategies in the space group $P\bar{3}m1$, with and without twinning, led to higher residual factors, significantly higher differential electron densities, and tremendous variation in isotropic displacement parameters, so these alternatives were rejected. Therefore, in keeping with the atomic distributions in EuGaGe and $Eu(Ga_{0.45}Ge_{0.55(2)})_2$, the five 6^3 nets per unit cell were assigned as follows: (i) two nets are

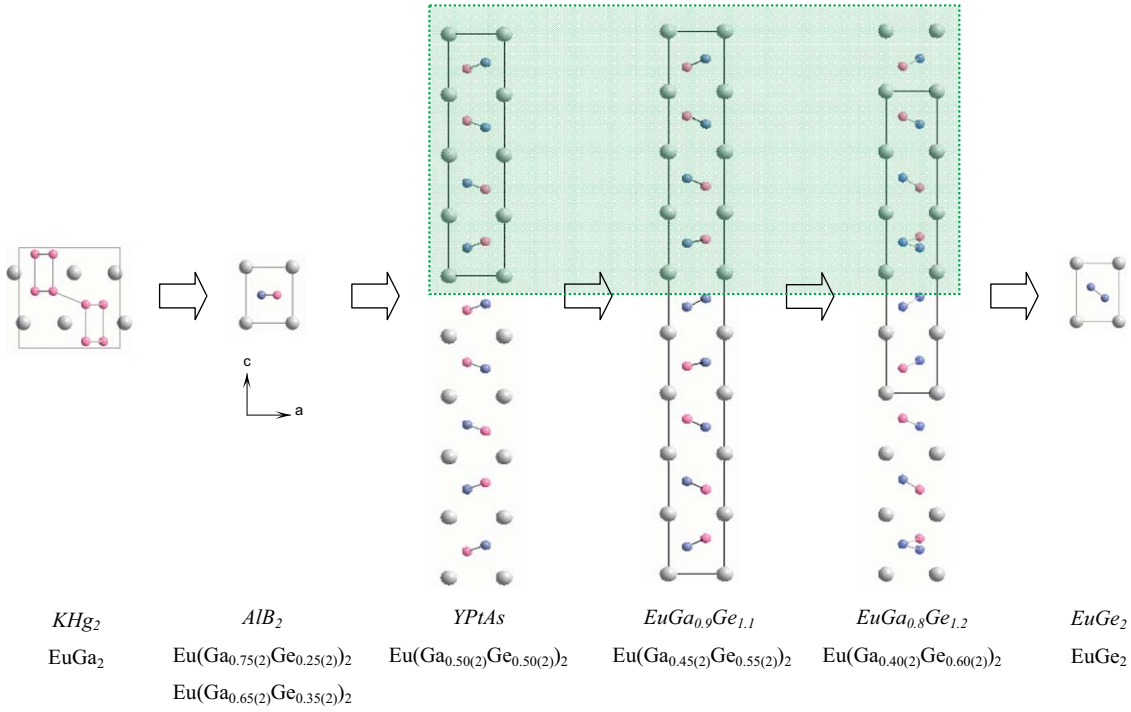

Fig. 5. Crystal structures along the $Eu(Ga_{1-x}Ge_x)_2$ ($0 \le x \le 1$) series. The structure types are given in italics. The shaded region emphasizes the YPtAs-type building blocks contained in the three phases EuGaGe, $EuGa_{0.9}Ge_{1.1}$, and $EuGa_{0.8}Ge_{1.2}$.

alternating [GaGe] layers; (ii) the net containing the split 2*i* site is an alternating [GaGe] layer with Ga atoms assigned to the 2*i* site; and (iii) the remaining two nets are each disordered 50:50 mixtures of [GaGe] and [Ge_2] nets. $Eu(Ga_{0.40}Ge_{0.60(2)})_2$ thus represents a 1:1 intergrowth between one YPtAs-type EuGaGe unit cell and one $EuGe_2$ cell, and can be formulated as [(EuGaGe)$_4$][$EuGe_2$] = "$Eu_5Ga_4Ge_6$" = $Eu(Ga_{0.40}Ge_{0.60})_2$. Furthermore, as in EuGaGe and $Eu(Ga_{0.45}Ge_{0.55(2)})_2$, the Ga···Ga distances between adjacent 6^3 [GaGe] nets are 3.678(1) and 3.873(1) Å. The crystallographic results for these two phases are summarized in the Supporting Information. Since our survey of the $Eu(Ga_{1-x}Ge_x)_2$ series is not exhaustive and the XPD patterns for each product do not show multiple phases, it is possible that other phases may exist in this ternary system.

A comparison of the structural features for the four Ge-rich phases $Eu(Ga_{1-x}Ge_x)_2$, summarized in Table 4, reveals some interesting trends that impact their electronic structures. As the Ge content increases from EuGaGe to $EuGe_2$, *a* decreases, *c* increases, and both *c*/*a* and volume per formula unit $Eu(Ga_{1-x}Ge_x)_2$ increase. The variations in unit cell parameters can be attributed primarily to the pyramidalization at the main group elements rather than changes in interatomic distances. Pyramidalization at each Ga/Ge site can be quantified by the angular deficiency of the sum of the three bond angles from 360°; the greater this deficiency, the more pyramidal is the local structure. The results in Table 4 indicate that pyramidalization increases as the Ge content increases in these Ge-rich $Eu(Ga_{1-x}Ge_x)_2$.

3.4. Magnetic susceptibilities of $Eu(Ga_{1-x}Ge_x)_2$

The temperature-dependent magnetic susceptibilities ($\chi = M/H$) and inverse susceptibilities ($1/\chi$) of three $Eu(Ga_{1-x}Ge_x)_2$ compounds ($x = 0.50(2)$, 0.55(2), 0.60(2)) are plotted in Fig. 7a for a field $\mu_0 H = 0.1$ T. We specifically targeted these samples for magnetic measurements to explore possible magnetic exchange interactions based on the extended periodicities along the *c*-axis. A small bump in $1/\chi$ of $Eu(Ga_{0.50(2)}Ge_{0.50(2)})_2$ (and an even smaller one in $1/\chi$ of $Eu(Ga_{0.45(2)}Ge_{0.55(2)})_2$) near 70 K is due to the ferromagnetic ordering of a trace of EuO impurity phase. All three compounds show Curie–Weiss behavior for temperatures above ca. 150 K. Fitting a linear equation to these $1/\chi$ data results in the following paramagnetic effective moments (μ_{eff}) and Weiss temperatures (θ_W): $Eu(Ga_{0.50}Ge_{0.50})_2$, $\mu_{eff} = 8.02(4)\,\mu_B$, $\theta_W = +9.3$ K; $Eu(Ga_{0.45}Ge_{0.55})_2$, $\mu_{eff} = 8.08(4)\,\mu_B$, $\theta_W = -2.1$ K; and $Eu(Ga_{0.40}Ge_{0.650})_2$, $\mu_{eff} = 8.08(4)\,\mu_B$, $\theta_W = +4.9$ K. The values of μ_{eff} are close to the value of 7.94 μ_B for the $^8S_{7/2}$ state of the $4f^7$ configuration of Eu, thus indicating clearly that Eu is divalent in these compounds, a feature that is also characteristic of Eu in EuT_xSi_{2-x} based on Mössbauer spectroscopy [44]. The Weiss temperatures are small and decrease and change sign with increasing *x*. This suggests weak ferromagnetic ($x = 0.50$) or antiferromagnetic ($x = 0.55$ and 0.60) leading interactions between Eu $S = \frac{7}{2}$ moments or eventually competing interactions.

Below ca. 100 K, the susceptibilities become dependent on the external magnetic field, which is partially due to the EuO impurity. At even lower temperatures, the susceptibility curves $\chi(T)$ of all three samples rise sharply and attain maxima at ca. 25 K ($x = 0.50$), ca. 22 K ($x = 0.55$), and ca. 14 K ($x = 0.60$) (temperatures are taken from $\chi(T)$ curves measured during cooling in a field of $\mu_0 H = 0.01$ T). Below these corresponding temperatures, the susceptibilities decrease slightly. These features are very broad, but, nevertheless, indicate a magnetic ordering of the Eu moments.

Isothermal magnetization curves recorded at 1.8 K are given in Fig. 7b. The magnetizations after cooling in zero field rise quickly at first and then slower; the $Eu(Ga_{0.50}Ge_{0.50})_2$ sample shows the fastest and strongest rise, which agrees with its positive Weiss temperature. All three $M(H)$ curves do not saturate at 7 T. For a full alignment of the Eu moments, 7.0 μ_B are expected. The magnetic hysteresis behavior for fields below ca. 1 T indicates that the magnetic structures of all three samples are basically antiferromagnetic but have significant ferromagnetic components.

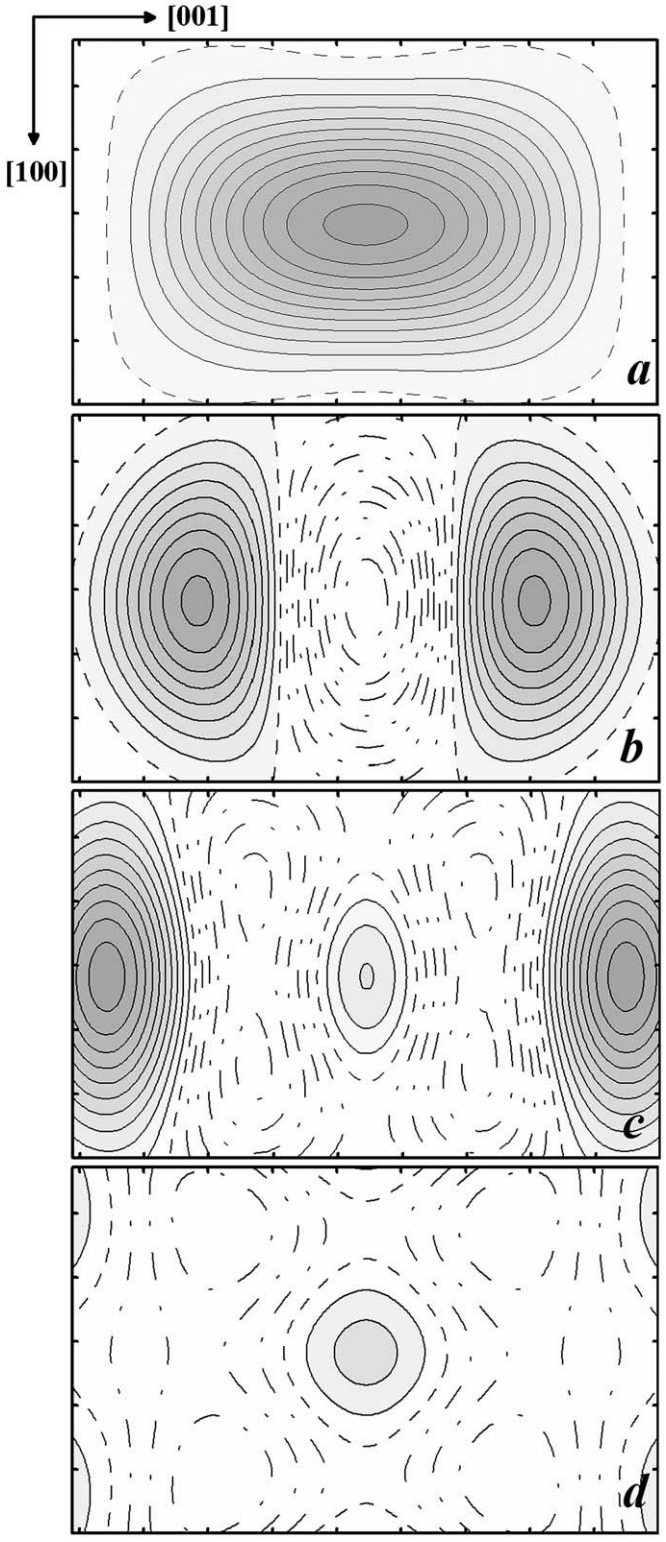

Fig. 6. Difference electron density for $Eu(Ga_{0.55}Ge_{0.45})_2$ (AlB_2-type) in the (0 1 0) plane at $y = 2/3$ in vicinity of the position 1/3 2/3 1/2: (a) without atoms in this position ($\Delta\rho = 5e^-Å^{-1}$); (b) Ga at $z = 1/2$ ($\Delta\rho = 5e^-Å^{-1}$); (c) Ga at $z = 0.56$ ($\Delta\rho = 0.5e^-Å^{-1}$); (d) Ga at $z = 1/2$ and $z = 0.5871$, occupations cf. Table S3 ($\Delta\rho = 0.1e^-Å^{-1}$). Zero line is dashed, positive difference density is shown by full lines, negative one-by dotted-dashed lines. The axes step is 0.2 Å.

Competing interactions may play a role in generating such complex behavior. The disorder of the Ga and Ge atoms possibly leads to the strong broadening of the magnetic ordering transitions. Similar magnetic data have been observed for several Eu*TX* phases [45] and the Eu*T*Mg ferromagnets [46].

3.5. Eu L_{III} XAS measurements

Sharp absorption maxima in XAS spectra (see Fig. 8) are observed at ca. 6977 eV for four $Eu(Ga_{1-x}Ge_x)_2$ ($x = 0.45(5)$, 0.50(2), 0.55(2), 0.60(2)) samples, which further confirms a $4f^7$ electronic configuration at the Eu atoms. Small shoulders are observed in these spectra at ca. 10 eV higher than the main absorption peak, which are assigned to small traces of Eu_2O_3 (electronic configuration $4f^6$, Eu^{3+}) in all three samples.

3.6. Electronic structure calculations

To examine the electronic structure and chemical bonding features that contribute to the structural trends and atomic distributions in $Eu(Ga_{1-x}Tt_x)_2$ (Tt = Si, Ge, $0 \le x \le 1$), TB-LMTO-ASA electronic structure calculations were carried out on selected models of the crystal structures. In particular, DOS and COHP curves were carefully analyzed to understand the observed homogeneity ranges of the AlB_2-type $Eu(Ga_{1-x}Tt_x)_2$ phases. For all systems, the DOS curves for the majority and minority spin states differed only slightly, so subsequent DOS curves illustrate their superposition; the Fermi level (E_F) is the energy reference in all curves. For valence electron counting purposes, the Eu atoms are considered divalent, which is supported by the magnetic susceptibility and XAS measurements discussed above. Since Ga is trivalent and the Tt atoms are tetravalent, the valence electron count per formula unit for $Eu(Ga_{1-x}Tt_x)_2$ is (8+2x) electrons, and thus varies from 8 to 10 electrons.

3.7. $Eu(Ga_{1-x}Si_x)_2$ (AlB_2-type)

Our experimental results concluded the stability range to be $0.18(2) \le x < 0.70(2)$ with statistical mixing of Ga and Si atoms on the 2*d* sites. These values correspond to 8.36(4)–9.40(4) valence electrons per $Eu(Ga_{1-x}Si_x)_2$ formula unit. To model this system for TB-LMTO calculations, we considered EuGaSi with planar, alternant 6^3 [GaSi] layers in three different stacking modes along the *c*-axis: (i) eclipsed stacking giving only Ga···Ga and Si···Si contacts; (ii) alternate stacking giving only Ga···Si contacts; and (iii) a 1:1 mixture of eclipsed and alternate stacking [18]. The calculated total electronic energy is lowest for model (ii) with just Ga–Si and Ga···Si first- and second-nearest-neighbor interactions (Fig. 9, top), by 0.14 and 0.75 eV/formula unit, respectively, with respect to models (iii) and (i). Thus, we utilized model (ii) for subsequent DOS and COHP analysis.

Fig. 9 (bottom) displays the DOS and COHP curves within 4 eV of the Fermi level (E_F) for 9-electron EuGaSi in model (ii). Throughout the entire DOS curve, significant mixing between valence orbitals of Eu, Ga, Si atoms is observed with no clear energy gaps. There is a pseudogap ca. 1 eV below E_F, the states below which have mostly Si and some Ga character, whereas the region just above this pseudogap is dominated by Eu valence 5*d* and 6*s* orbitals. The position of this pseudogap in the DOS curve corresponds to a band filling of 8 valence electrons per formula unit, which also nearly matches the top of Ga–Si bonding states shown in the adjacent COHP curve. The Ga–Si COHP curves for σ and π overlaps are optimized at 8.4 valence electrons, and remain essentially nonbonding until ca. 9.2 valence electrons. Above this electron count, the Ga–Si orbital interactions develop significant σ^* character. The COHP curve for Ga···Si second nearest-neighbor contacts along the *c*-axis show weak, essentially nonbonding orbital interactions (the curve is magnified by 10), but has

Table 3
Crystallographic data for $Eu(Ga_{1-x}Ge_x)_2$.

Composition:	$Eu(Ga_{0.75}Ge_{0.25})_2$	$Eu(Ga_{0.65}Ge_{0.35})_2$	$Eu(Ga_{0.55}Ge_{0.45})_2$	$Eu(Ga_{0.45}Ge_{0.55})_2$	$Eu(Ga_{0.40}Ge_{0.60})_2$
Formula weight ($g\,mol^{-1}$)	293.20	293.40	293.60	294.56	294.85
Space group	*P*6/*mmm* (no. 191)	*P*6/*mmm* (no. 191)	*P*6/*mmm* (no. 191)	$P\bar{3}m1$ (no. 164)	$P\bar{6}m2$ (no. 187)
$(c/a)^*$	1.0739	1.0749	*1.079*	1.0681	1.0857
Vol ($Å^3$)	73.46(1)	72.06(1)	70.95(5)	639.02(3)	356.34(2)
Z	1	1	1	9	5
Density calc. ($g\,cm^{-3}$)	6.62	6.76	6.88	6.864	6.87
Diffractometer	STOE IPDS	SMART Apex	STOE STADI 4	SMART Apex	SMART Apex
2θ range (deg)	11.00–70.60	8.9–69.88	8.95-64.78	2.00–56.8	1.76–55.84
Index ranges	$-6\le h\le 6$, $-6\le k\le 6$, $-5\le l\le 7$	$-6\le h\le 6$, $-6\le k\le 6$, $-7\le l\le 7$	$-6\le h\le 5$, $0\le k\le 6$, $-6\le l\le 6$	$-5\le h\le 5$, $-3\le k\le 5$, $-51\le l\le 53$	$-5\le h\le 5$, $-5\le k\le 5$, $-30\le l\le 29$
Reflections collected	1377	712	573	3913	3075
Independent reflections	92 [$R_{init}=0.122$]	82 [$R_{init}=0.094$]	75 [$R_{init}=0.084$]	742 [$R_{init}=0.089$]	419 [$R_{init}=0.025$]
Data/parameters	92/7	86/7	71/11	742/42	419/27
GOF on F^2	1.192	1.073	0.850	0.089	1.125
Residuals [$I>2\sigma(I)$]	$R_1=0.031$, $wR_2=0.063$	$R_1=0.034$ $wR_2=0.073$	$R_1=0.024$, $wR_2=0.036$	$R_1=0.048$, $wR_2=0.108$	$R_1=0.028$, $wR_2=0.052$
Residuals (all data)	$R_1=0.035$, $wR_2=0.064$	$R_1=0.035$ $wR_2=0.073$	$R_1=0.028$, $wR_2=0.037$	$R_1=0.131$, $wR_2=0.142$	$R_1=0.038$, $wR_2=0.056$
Largest differential density ($e^-/Å^3$)	2.38/−1.55	2.23/−2.75	0.24/−0.45	2.188/−2.686	0.94/−1.14

Table 4
Selected interatomic distances and angular deficiencies at anionic sites in Ge-rich $Eu(Ga_{1-x}Ge_x)_2$ phases.

Composition:	$Eu(Ga_{0.50(2)}Ge_{0.50(2)})_2$		$Eu(Ga_{0.45(2)}Ge_{0.55(2)})_2$	$Eu(Ga_{0.40(2)}Ge_{0.60(2)})_2$	$EuGe_2$ [33]
d(Ga-Ge) (Å)	2.531(1)	1st layer[a]	2.533(1)	2.511(1)	2.551
		2nd layer	2.530(1)	2.556(1)	
		3rd layer	2.528(1)	2.487(1)	
		4th layer	2.473(1)		
		5th layer[b]	2.535(1)		
Angular deficiency (°)[c]	15.9	1st layer	18.5	15.5	39.0
		2nd layer	16.4	24.8	
		3rd layer	16.5	10.2	
		4th layer	4.3		
		5th layer	17.8		

[a] The order of layers starts from the origin of a unit cell.
[b] Due to the inversion center located in the 5th layer of a unit cell, five out of nine layers were sufficient to describe structural details.
[c] Angular deficiency from 360° at each site indicates the tendency of pyramidalization at a given site.

repulsive character just below the pseudogap at 8 valence electrons. Furthermore, the Eu–Ga and Eu–Si COHP curves are slightly bonding in the Ga–Si nonbonding region. Therefore, within a rigid-band approximation applied to the DOS and based on these various COHP curves, $Eu(Ga_{1-x}Si_x)_2$ can tolerate a range of valence electron counts from ca. 8.4 to 9.2 electrons without significantly disrupting the nearest-neighbor Ga–Si interactions and the planarity of the 6^3 $[Ga_{1-x}Si_x]$ nets. This range of electron counts agrees reasonably well with the experimental range; poor agreement with the observed upper bound (Si-rich end) may be due to the limitations of the rigid-band approximation applied in this analysis as well as an increased tendency toward puckering of the 6^3 nets for larger *x* values.

Therefore, to assess the theoretical preference of planar vs. puckered 6^3 nets in Si-rich $Eu(Ga_{1-x}Si_x)_2$ phases, optimized structures of $EuSi_2$ were determined using the *VASP* code for three different structure types: the tetragonal $ThSi_2$-type; the hexagonal AlB_2-type; and the trigonal $EuGe_2$-type. Accordingly, the $ThSi_2$-type is preferred, in agreement with experiment, by 61 meV/$EuSi_2$ over the $EuGe_2$-type, and by 164 meV/$EuSi_2$ over the AlB_2-type. Furthermore, the theoretical lattice constants of the $ThSi_2$-type structure are in excellent agreement with experimental values: $a_{VASP}=4.318$ Å, $c_{VASP}=13.708$ Å; $a_{EXP}=4.3065(4)$ Å, $a_{EXP}=13.683(1)$ Å [40]. For the other alternatives, the optimized lattice constants are as follows: for the $EuGe_2$-type, $a_{VASP}=3.956$ Å, $c_{VASP}=4.849$ Å, $c/a=1.226$, $V=65.715\,Å^3$; for the AlB_2-type, $a_{VASP}=4.080$ Å, $c_{VASP}=4.439$ Å, $c/a=1.088$, $V=63.989\,Å^3$. These theoretical results are especially interesting, in light of the results presented in Table 1, and strongly suggest that the $Eu(Ga_{0.25}Si_{0.75})_2$ phase observed in the two-phase product (Fig. 1e) contains puckered 6^3 nets. To establish the homogeneity range for this puckered variant, COHP analysis of the Si–Si contacts in the 6^3 nets based on TB-LMTO calculations of the optimized $EuGe_2$-type $EuSi_2$ (see Supporting Information) revealed maximum bonding character at ca. 8.30 valence electrons with Si–Si nonbonding character ranging up to ca. 9.70 valence electrons. Thus, as the tendency toward puckering of the 6^3 $[Ga_{1-x}Si_x]$ net increases, the number of valence electrons also increases and extends the observed range above based on EuGaSi. The *VASP* calculations also shed light on the unusual lattice parameters refined for the AlB_2-type phase in the sample loaded with $x=0.84$ (see Table 1): the calculated *c*/*a* ratio for the $EuGe_2$-type $EuSi_2$ is significantly larger than that of the AlB_2-type $EuSi_2$. Therefore, in addition to the arguments based on experimental evidence and these computational results, we propose a Si-rich region in the $Eu(Ga_{1-x}Si_x)_2$ system that adopts the trigonal $EuGe_2$-type structure with puckered $[Ga_{1-x}Si_x]$ nets. Further results of *VASP* calculations are available in the Supporting Information.

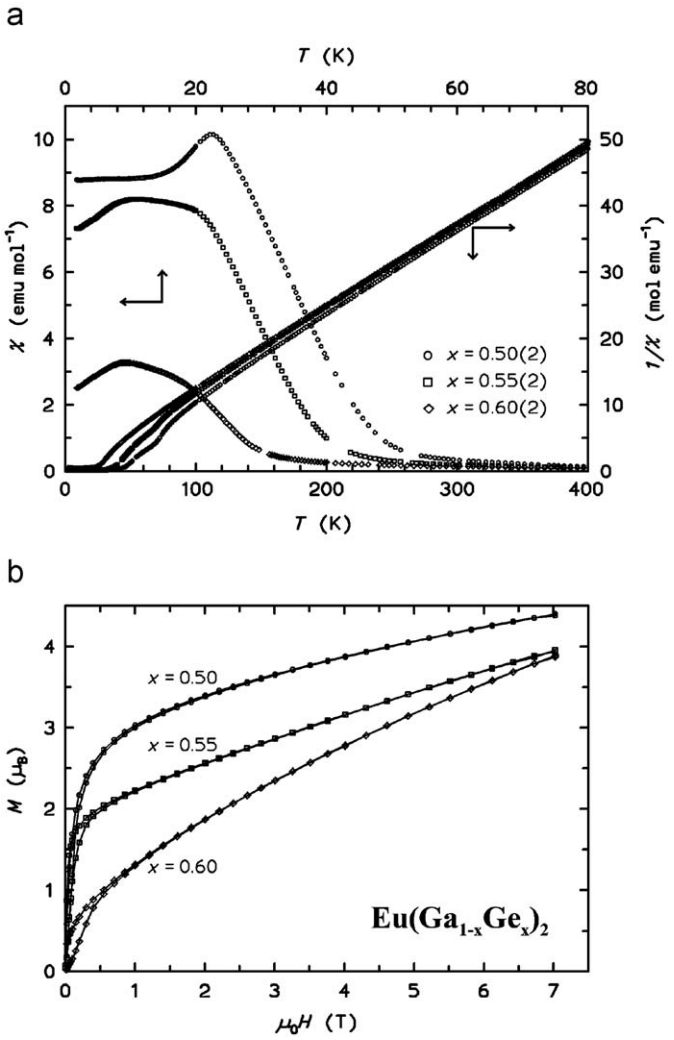

Fig. 7. (a) Temperature-dependent magnetic susceptibilities $\chi(T)$ (left and upper axes) and inverse magnetic susceptibilities $1/\chi(T)$ (right and lower axes) for $Eu(Ga_{1-x}Ge_x)_2$ with $x = 0.50(2)$, 0.55(2), and 0.60(2). (b) Isothermal magnetization curves $M(H)$ up to 7.0 T at $T = 1.8$ K for the same samples.

3.8. $Eu(Ga_{1-x}Ge_x)_2$ (AlB_2-type)

Experimental results indicate the stability range is limited to $x < 0.50$. Although we did not attempt to determine the precise upper or lower boundaries of this phase region, there is certainly a homogeneity width between at least $x = 0.25$ and ca. 0.40. As in the silicides, we considered "EuGaGe" with only Ga–Ge and Ga · · · Ge first- and second-nearest-neighbor interactions for TB-LMTO calculations.

DOS and COHP curves are illustrated in Fig. 10. While most features of these curves are similar to those of AlB_2-type EuGaSi, a noticeable difference is seen in the nearest-neighbor Ga–Ge COHP curve. Whereas the Ga–Si COHP curve of EuGaSi shows essentially nonbonding states between ca. 8.4 and 9.2 valence electrons per EuGaSi, the corresponding Ga–Ge COHP curve of "EuGaGe" is optimized at ca. 8.25 valence electrons and clearly shows antibonding states above 8.5 valence electrons. Decomposing the Ga–Ge interactions into σ and π overlap components shows this feature to arise from σ^* overlap. Therefore, on the basis of COHP analyses, the upper limit of the homogeneity range for $Eu(Ga_{1-x}Ge_x)_2$ should not exceed that of $Eu(Ga_{0.50}Ge_{0.50})_2$ with 9.0 valence electrons, but can extend to a lower bound of ca. 8.3 valence electrons, i.e., $Eu(Ga_{0.85}Ge_{0.15})_2$. The two experimentally observed compounds adopting the AlB_2-type structures have, respectively, 8.5 and 8.7 valence electrons. Furthermore, the crystallographic results for $Eu(Ga_{0.55}Ge_{0.45(2)})_2$ suggested puckered 6^3 nets, as in the $EuGe_2$-type.

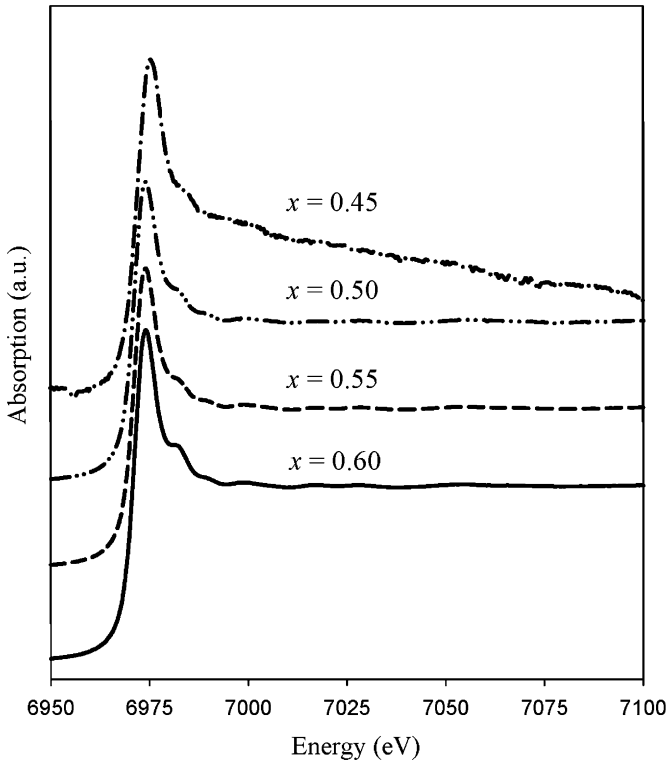

Fig. 8. XAS spectra of $Eu(Ga_{1-x}Ge_x)_2$ ($x = 0.45(5)$, 0.50(2), 0.55(2), 0.60(2)).

3.9. Ge-rich $Eu(Ga_{1-x}Ge_x)_2$

From the structures of the four known examples, $x = 0.50$, 0.55, 0.60, and 1.00, these phases may be formulated as $[EuGaGe]_{2-2x}[EuGe_2]_{2x-1}$ to emphasize the intergrowth structures detected in the $x = 0.55$ and 0.60 phases. The theoretical electronic structure of EuGaGe was previously discussed, and its DOS and COHP curves show features resembling those found for the AlB_2-type "EuGaGe" in Fig. 10 (see Fig. 7 of Ref. [18]). However, there is one distinct difference in the DOS curves between the AlB_2-type and YPtAs-type structures: the pseudogap close to 8 valence electrons observed in the AlB_2-type DOS is less pronounced in the YPtAs-type DOS, which is caused by the overlapping Eu 5*d* bands (see Supporting Information). Also, the Ga–Ge COHP curves in the two structure types are different. The Ga–Ge COHP curve [18] for the YPtAs-type structure is optimized at 8.50 valence electrons per formula unit (ca. 0.6 eV below E_F) and remains essentially nonbonding up to ca. 9.25 valence electrons (ca. 0.3 eV above E_F); in AlB_2-type "EuGaGe," the optimal range is ca. 8.3–9.0 valence electrons. The difference between these two nearest-neighbor Ga–Ge COHP curves can be attributed to the different *s*–*p* hybridization occurring at the Ga and Ge atoms in the puckered vs. planar 6^3 nets as well as the different involvement of Eu 5*d* states. Previous computational studies invoking analysis by electron localization functions indicated that the Eu 5*d* orbitals are involved in multi-center orbital interactions with Ga 4*s* and 4*p* orbitals, interactions, which contribute to the puckering of the 6^3 nets and their relative orientations [18].

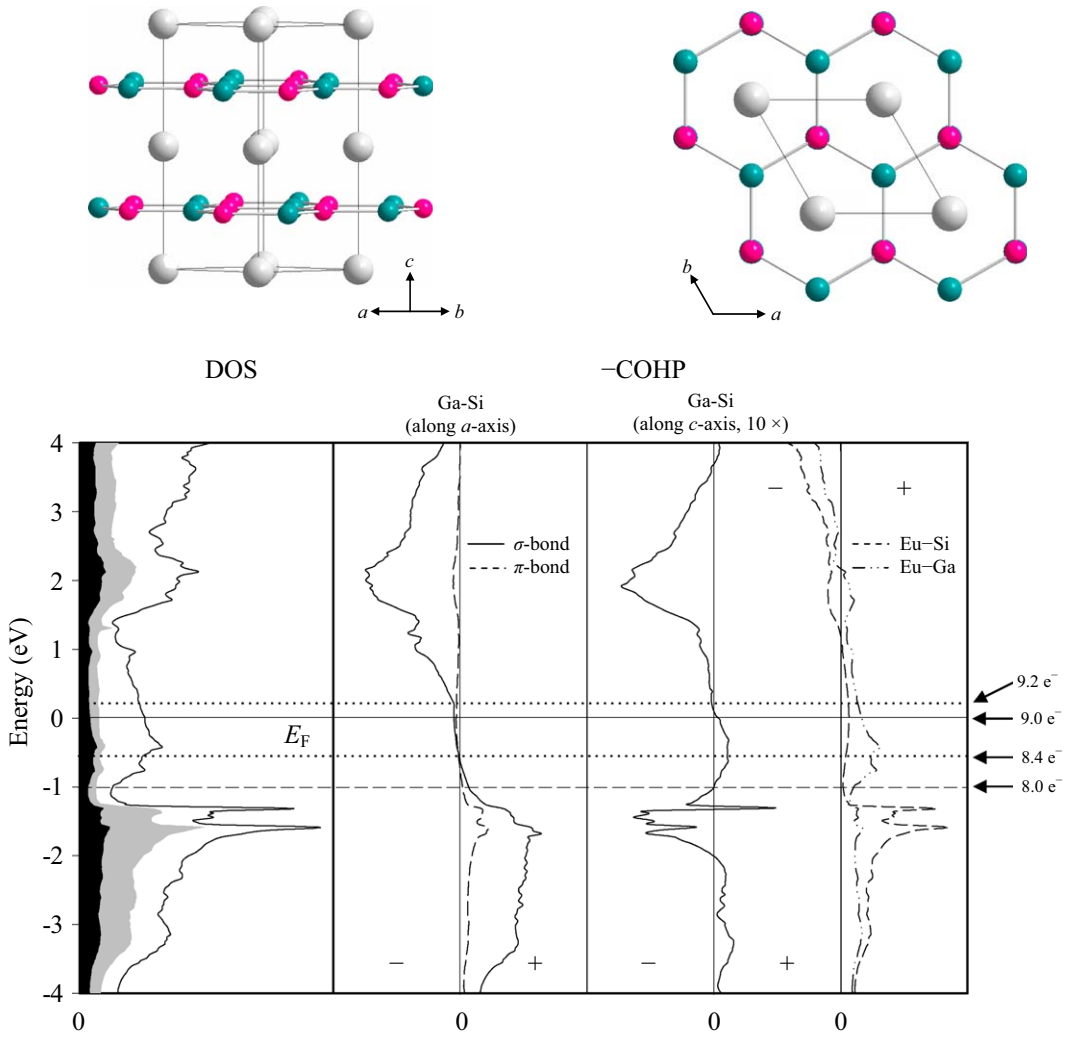

Fig. 9. (Top) Structural model of AlB_2-type $Eu(Ga_{0.50}Si_{0.50})_2$. Eu: gray; Ga: red; Si: green. (Bottom) DOS and COHP curves for AlB_2-type $Eu(Ga_{0.50}Si_{0.50})_2$. (Left) Total DOS (solid line), Eu PDOS (white region) and Si PDOS (gray region), and Ga PDOS (black region). (Right) Ga–Si (along the *a*-axis, *c*-axis), Eu–Si, and Eu–Ga COHP curves. The Fermi level is indicated by the solid line. Other Fermi levels for various valence electron counts are indicated. (For interpretation of the references to color in this figure legend, the reader is referred to the web version of this article).

$Eu(Ga_{0.45}Ge_{0.55(2)})_2$ contains 8 [GaGe] and 1 [Ge_2] puckered 6^3 nets, and given this description, its DOS curve, shown in Fig. 11, is similar to the DOS curve of EuGaGe [18].The strongest peak occurs at ca. 1.7 eV below E_F, while there are no apparent pseudogaps. There is more Ge 4*p* orbital contribution to the total DOS than Eu 5*d* orbitals or Ga 4*p* orbitals below E_F because of the Ge-rich composition and relative electronegativities, while Eu 5*d* orbital contributions become greater near and above E_F. The intergrowth character of this structure is validated by evaluating the number of valence electrons assigned to each 6^3 net as determined by the integrated total DOS curve: the net assigned as [Ge_2] gives 9.98 electrons (as in $EuGe_2$), while the others assigned as [GaGe] integrate to 8.98–9.01 electrons (as in EuGaGe). These results are listed in detail in the Supporting Information.

The Ga–Ge COHP curve for $Eu(Ga_{0.45}Ge_{0.55(2)})_2$ is optimized at ca. 8.6 valence electrons per [GaGe] 6^3 net (ca. 0.5 eV below E_F), and shows nonbonding character up to ca. 9.6 valence electrons (ca. 0.7 eV above E_F), which is similar to that of EuGaGe. The Ge–Ge COHP curve for the puckered hexagonal layer consisting of entirely Ge atoms is optimized at ca. 1.4 eV below E_F, and shows antibonding states at E_F [42]. This Ge-only layer can be compared with Ge layers in $EuGe_2$, for which the Ge–Ge COHP curve is nearly optimized at E_F with 10 valence electrons. The difference between these COHP curves can be understood from different local environments surrounding this Ge layer. The 6^3 [Ge_2] layer in $Eu(Ga_{0.45}Ge_{0.55(2)})_2$ does not pucker as much (angular deficiency is 17.5°; see Table 4) as it does in $EuGe_2$ (angular deficiency is 39.0°) because of the spatial restriction in $Eu(Ga_{0.45}Ge_{0.55})_2$ as measured by the $(c/a)^*$ ratios (see Table 1). The wider separation between 6^3 nets in $EuGe_2$ than in $Eu(Ga_{0.45}Ge_{0.55})_2$ causes this structural effect. Furthermore, and as a result, a shorter Ge–Ge bond distance is observed in $Eu(Ga_{0.45}Ge_{0.55})_2$, i.e., 2.527 Å for $Eu(Ga_{0.45}Ge_{0.55})_2$ and 2.552 Å for $EuGe_2$ [42], and can explain the antibonding character of this Ge–Ge COHP curve at E_F.

3.10. $Eu(Ga_{1-x}Tt_x)_2$: Si vs. Ge

The differences between the structural and phase behavior of $Eu(Ga_{1-x}Si_x)_2$ and $Eu(Ga_{1-x}Ge_x)_2$ are subtle yet distinct. In particular, the occurrence of AlB_2-type phases shows different compositional ranges in the two cases: in the silicides, the range is wide ($0.18(2) \le x < 0.70(2)$), which corresponds to 8.36(4)–9.40(4) electrons; in the germanides, the range is narrower,

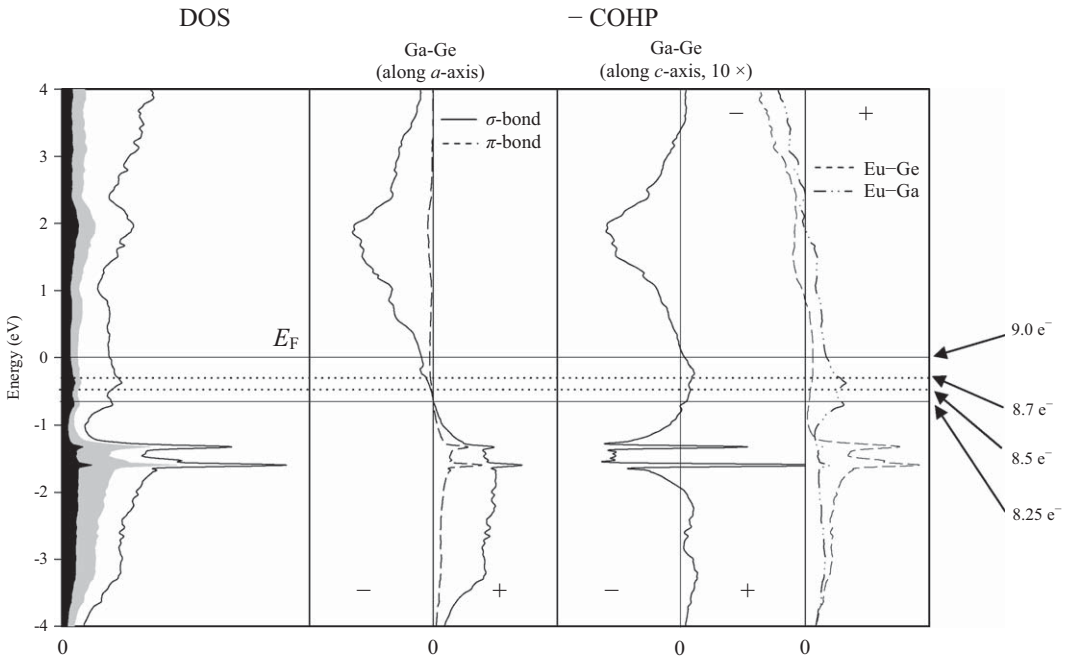

Fig. 10. DOS and COHP curves for AlB_2-type $Eu(Ga_{0.50}Ge_{0.50})_2$ to model $Eu(Ga_{1-x}Ge_x)_2$ ($0.25 \leq x \leq 0.35$). (Left) Total DOS (solid line), Eu PDOS (white region), Ge PDOS (gray region), and Ga PDOS (black region). (Right) Ga–Ge (along the *a*-axis, *c*-axis), Eu–Ge, and Eu–Ga COHP curves. The Fermi level for $Eu(Ga_{0.50}Ge_{0.50})_2$ is indicated by the solid line. Other Fermi levels for various valence electron counts are indicated.

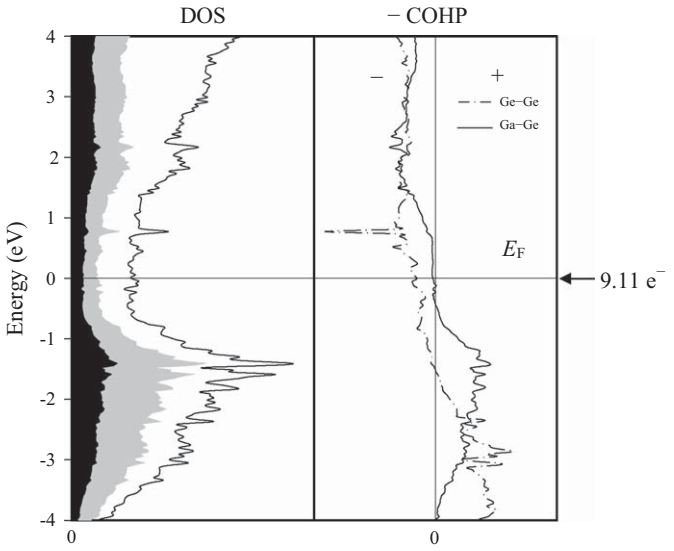

Fig. 11. DOS and COHP curves for $Eu(Ga_{0.45}Ge_{0.55})_2$. (Left) Total DOS (solid line), Eu PDOS (white region), Ge PDOS (gray region), and Ga PDOS (black region). (Right) Ga–Ge, Eu–Ga, and Eu–Ge COHP curves. The Fermi level is indicated by the solid line.

Table 5
Interaction energies (ΔE), estimated by Hückel calculations, for Ga–Si and Ga–Ge σ and π bonds for sp^2 and sp^3 hybridized Ga, Si, and Ge, and estimated energies for 8-electron and 9-electron configurations for 6^3 nets.

	$\Delta E_\sigma(sp^2)$	ΔE_π	$\Delta E_\sigma(sp^3)$	sp^2/π	(eV)	sp^3	(eV)
Ga–Si	8.63	1.83	7.49	$8e^-$ $(\sigma)^6(\pi)^2$	−55.45	$8e^-$ $(\sigma)^8$	**−59.94**
				$9e^-$ $(\sigma)^6(\pi)^2(\pi^*)^1$	**−53.63**	$9e^-$ $(\sigma)^8(\sigma^*)^1$	−52.45
Ga–Ge	7.91	1.56	7.11	$8e^-$ $(\sigma)^6(\pi)^2$	−50.56	$8e^-$ $(\sigma)^8$	**−56.88**
				$9e^-$ $(\sigma)^6(\pi)^2(\pi^*)^1$	−49.00	$9e^-$ $(\sigma)^8(\sigma^*)^1$	**−49.77**

Boldfaced values indicate lower energy for each electron count and bond type.

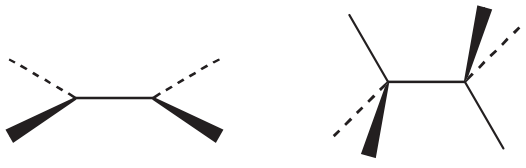

1 **2**

(∼0.25 ≤ *x* ≤ ∼0.45), or ∼8.5–8.9 electrons. For more electron-rich cases, the germanides exhibit puckered 6^3 nets [41]. Also, the binary tetrelides, $EuSi_2$ and $EuGe_2$, are distinctly different and show two different modes of disrupting the π-antibonding interactions [3,47]. In $EuSi_2$, all Si atoms are locally trigonally planar by three Si atoms, but the planes of adjacent Si atoms are perpendicular to each other. On the other hand, all Ge atoms in $EuGe_2$ are trigonally pyramidally coordinated by three Ge atoms to create puckered 6^3 nets. Both of these observations suggest that under slightly reduced environments, Si prefers sp^2 hybridization while Ge prefers sp^3 hybridization.

We can demonstrate this difference between Si and Ge semi-quantitatively in $Eu(Ga_{1-x}Tt_x)_2$ by estimating the relative energetics of Ga–*Tt* σ- and π-interactions based on either sp^2 (**1**) or sp^3 (**2**) hybridized Ga and *Tt* atoms for 8- and 9-electron systems within simple Hückel theory [48]. For these calculations, model structures $[H_2Ga{-}TtH_2]$ (**1**) and $[H_3Ga{-}TtH_3]$ (**2**) were employed using covalent radii to set interatomic distances. All atoms were modeled by Slater-type orbitals and their atomic orbital energies were given by configuration energies [49], which indicate that Ge is more electronegative than Si. The specific Ga–*Tt* σ- and π-interactions were then determined by averaging the differences between bonding/antibonding orbitals in $[H_nGa{-}TtH_n]$ ($n = 2, 3$)

and the orbitals of the isolated fragments, [GaH_n] and [TtH_n] ($n = 2, 3$). These results are summarized in Table 5. As expected, Ga–Si interactions are stronger than Ga–Ge. The estimated relative energies associated with 8-electron and 9-electron planar (sp^2) or puckered (sp^3) 6^3 [$GaTt$] nets are evaluated using these interaction energies applied to the appropriate electronic configuration, which is also listed in Table 5. This semi-quantitative analysis indicates that at $9e^-$, local sp^2 hybridization is favored for the silicides whereas local sp^3 hybridization is preferred for the germanides. For $8e^-$, local sp^3 hybridization is preferred for both silicides and germanide systems.

4. Summary

A total of 16 Eu($Ga_{1-x}Tt_x$)$_2$ samples (Tt = Si, Ge, $0 \le x \le 1$) were synthesized using high temperature methods and characterized using powder and single-crystal X-ray diffraction. According to the magnetic susceptibilities and X-ray absorption spectra of certain examines, Eu exhibits divalent behavior in these phases. The Eu($Ga_{1-x}Si_x$)$_2$ series adopts the AlB_2-type structure over a wide composition range covering ca. 8.4–9.5 valence electrons per formula unit, which can be understood by orbital interactions within each 6^3 net. As the Si content increases, there is an increasing tendency for the hexagonal nets to pucker. On the other hand, Eu($Ga_{1-x}Ge_x$)$_2$ samples adopt the AlB_2-type for Ge-poor compositions, ranging between ca. 8.5 and 8.9 valence electrons per formula unit. On the Ge-rich side, however, puckered 6^3 nets develop in EuGaGe and $EuGe_2$, as well as two intergrowth structures of these two. The structural behavior of these silicides and germanides can be qualitatively understood on the differences in atomic sizes and electronegativities coupled with the observed valence electron counts.

Acknowledgments

This work was supported by NSF DMR 02-41092 and 06-05949. The authors are grateful to Dr. Warren Straszheim for the EDXS measurements and Stefan Hückmann for powder diffraction measurements. G.J.M., T.-S.Y. and J.T.Z. also thank the Max-Planck Society for the research fellowships.

Supporting Information Available: X-ray crystallographic files in CIF format, atomic coordinates and equivalent displacement parameters for Eu($Ga_{1-x}Ge_x$)$_2$ ($x = 0.25(2)$, 0.35(2), 0.45(5), 0.50(2), 0.55(2), 0.60(2)), Wigner-Seitz (WS) atomic sphere radii of elements used for LMTO calculations, computational details and energy comparison for two "$EuSi_2$" models, calculated IDOS values for Eu($Ga_{0.45}Ge_{0.55}$)$_2$, selected powder X-ray diffraction patterns of Eu($Ga_{1-x}Si_x$)$_2$, the Si-Si COHP curve of the relaxed $EuGe_2$-type "$EuSi_2$", and band structure of Eu($Ga_{0.5}Ge_{0.5}$)$_2$ with fatband contributions of Eu 5d orbitals. This material is available free of charge via the Internet at http://pubs.acs.org.

Appendix 1. Supporting Information

Supplementary data associated with this article can be found in the online version at doi:10.1016/j.jssc.2009.06.032.

References

[1] J.H. Westbrook, R.L. Fleisher (Eds.), Intermetallic Compounds: Principle and Practices, Wiley, New York, 1995.
[2] R. Nesper, Prog. Solid State Chem. 20 (1990) 1.
[3] G.J. Miller, in: S.M. Kauzlarich (Ed.), Chemistry, Structure, and Bonding of Zintl Phases and Ions, VCH Publishers, New York, 1996, p. 1.
[4] [a] H. Schäfer, Ann. Rev. Mater. Sci. 5 (1985) 1;
[b] H. Schäfer, B. Eisenmann, W. Müller, Angew. Chem. 85 (1973) 742.
[5] G.J. Miller, C.-S. Lee, W. Choe, in: G. Meyer (Ed.), Highlights in Inorganic Chemistry, Wiley-VCH, Heidelberg, 2002, p. 21.
[6] R. Dronskowski, P. Blöchl, J. Phys. Chem. 97 (1993) 8617.
[7] R. Hughbanks, R. Hoffmann, J. Am. Chem. Soc. 105 (1983) 3528.
[8] M.T. Klem, J.T. Vaughy, J.G. Harp, J.D. Corbett, Inorg. Chem. 40 (2001) 7020.
[9] O. Sichevych, M. Kohout, W. Schnelle, H. Borrmann, R. Cardoso Gil, M. Schmidt, U. Burkhardt, Yu. Grin, Inorg. Chem. 48 (2009) 6261.
[10] D. Gout, E. Benbow, O. Gourdon, G.J. Miller, J. Solid State Chem. 176 (2003) 538.
[11] G.Q. Huang, M. Liu, L.F. Chen, D.Y. Xing, Physica C 423 (2005) 9.
[12] M. Imai, E. Abe, J. Ye, K. Nishida, T. Kimura, K. Honma, H. Abe, H. Kitazawa, Phys. Rev. Lett. 87 (2001) 077003.
[13] M. Imai, K. Nishida, T. Kimura, H. Abe, Appl. Phys. Lett. 80 (2002) 1019.
[14] M. Imai, K. Nishida, T. Kimura, H. Kitazawa, H. Abe, H. Kito, K. Yoshii, Physica C 382 (2002) 361.
[15] B. Lorenz, J. Lenzi, J. Cmaidalka, R.L. Meng, Y.Y. Sun, Y.Y. Xue, C.W. Chu, Physica C 383 (2002) 191.
[16] J. Nagamatsu, N. Nakagawa, T. Muranaka, Y. Zenitani, J. Akimitsu, Nature 410 (2001) 63.
[17] M.J. Evans, G.P. Holland, J.P. Garcia-Garcia, U. Häussermann, J. Am. Chem. Soc. 130 (2008) 12139.
[18] T.-S. You, Yu. Grin, G.J. Miller, Inorg. Chem. 46 (2007) 8801.
[19] T.-S. You, S. Lidin, O. Gourdon, Y. Wu, G.J. Miller, Inorg. Chem. 48 (2009) 6380.
[20] T.-S. You, G.J. Miller, Inorg. Chem. 48 (2009) 6391.
[21] K.H.J. Buschow, D.B. Mooij, J. Less-Common Met. 97 (1984) L5.
[22] A.R. Miedema, J. Less-Common Met. 46 (1976) 167.
[23] O. Sichevych, R. Cardoso-Gil, Yu. Grin, Z. Kristallogr. NCS 221 (2006) 261.
[24] B.A. Hunter, C.J. Howard, Rietica, Australian Nuclear Science and Technology Organization, Menai, Australia, 2000.
[25] XRD single crystal software. Bruker Analytical X-ray System: Madison, WI, 2002.
[26] X-SHAPE, Program for numeric absorption, version 1.03; Stoe & Cie: Darmstadt, Germany, 1998.
[27] SHELXTL, version 5.1; Bruker AXS Inc., Madison, WI, 1998.
[28] L.G. Akselrud, P.Yu. Zavalii, Yu. Grin, V.K. Pecharski, B. Baumgartner, E. Wölfel, Mater. Sci. Forum 133–136 (1993) 335.
[29] J. Emsley, The Elements, Clarendon press, Oxford, 1998.
[30] O.K. Andersen, Phys. Rev. B 34 (1986) 2439.
[31] O.K. Andersen, O. Jepsen, Phys. Rev. Lett. 53 (1984) 2571.
[32] O.K. Andersen, O. Jepsen, D. Glötzel, in: F. Bassani, F. Fumi, M.Tosi (Eds.), Highlights of Condensed Matter Theory, New York, North-Holland, Lambrecht, W. R. L., 1985.
[33] O. Jepsen, O.K. Andersen, Z. Phys. B 97 (1995) 35.
[34] P.E. Blöchl, O. Jepsen, O.K. Andersen, Phys. Rev. B 49 (1994) 16223.
[35] G. Kresse, J. Hafner, Phys. Rev. B 47 (1993) RC558.
[36] G. Kresse, J. Furthmüller, Phys. Rev. (1996) 11169.
[37] G. Kresse, J. Furthmüller, Comput. Mater. Sci. 6 (1996) 15.
[38] D. Vanderbilt, Phys. Rev. B 41 (1990) 7892.
[39] G. Kresse, J. Hafner, J. Phys.: Condens. Matter 6 (1994) 824.
[40] J. Evers, G. Oehlinger, A. Weiss, F. Hulliger, J. Less-Common Met. 90 (1983) L19.
[41] R.-D. Hoffmann, R. Pöttgen, Z. Kristallogr. 216 (2001) 127.
[42] S. Bobev, E.D. Bauer, J.D. Thompson, J.L. Sarrao, G.J. Miller, B. Eck, R. Dronskowski, J. Solid State Chem. 177 (2004) 3545.
[43] E.I. Gladyshevsky, Dopl. Akad. Nauk Ukr. RSR 2 (1964) 209.
[44] I. Mayer, I. Felner, J. Solid State Chem. 8 (1973) 355.
[45] R. Pöttgen, D. Johrendt, Chem. Mater. 12 (2000) 875.
[46] D. Johrendt, G. Kotzyba, H. Trill, B.D. Mosel, H. Eckert, Th. Fickenscher, R. Pöttgen, J. Solid State Chem. 164 (2002) 201.
[47] C. Zheng, R. Hoffmann, Inorg. Chem. 28 (1989) 1074.
[48] J.K. Burdett, Molecular Shapes, Wiley-Interscience, New York, 1980.
[49] L.C. Allen, J. Am. Chem. Soc. 111 (1989) 9003.